Computers & Geosciences 89 (2016) 118–131

Contents lists available at ScienceDirect

Computers & Geosciences

journal homepage: www.elsevier.com/locate/cageo

Research paper

# A new method for automated discontinuity trace mapping on rock mass 3D surface model

Xiaojun Li, Jianqin Chen, Hehua Zhu *

*Department of Geotechnical Engineering, Tongji University, 1239 Siping Road, Shanghai 200092, China*

ARTICLE INFO

*Article history:*
Received 20 August 2015
Received in revised form
12 December 2015
Accepted 13 December 2015
Available online 17 December 2015

*Keywords:*
Rock mass
Discontinuity
Automated trace mapping
3D point clouds

ABSTRACT

This paper presents an automated discontinuity trace mapping method on a 3D surface model of rock mass. Feature points of discontinuity traces are first detected using the Normal Tensor Voting Theory, which is robust to noisy point cloud data. Discontinuity traces are then extracted from feature points in four steps: (1) trace feature point grouping, (2) trace segment growth, (3) trace segment connection, and (4) redundant trace segment removal. A sensitivity analysis is conducted to identify optimal values for the parameters used in the proposed method. The optimal triangular mesh element size is between 5 cm and 6 cm; the angle threshold in the trace segment growth step is between 70° and 90°; the angle threshold in the trace segment connection step is between 50° and 70°, and the distance threshold should be at least 15 times the mean triangular mesh element size. The method is applied to the excavation face trace mapping of a drill-and-blast tunnel. The results show that the proposed discontinuity trace mapping method is fast and effective and could be used as a supplement to traditional direct measurement of discontinuity traces.



## 1. Introduction

Discontinuity trace mapping is one of the fundamental tasks for rock mass characterization. Fracture size information (e.g., fracture trace length distribution and discontinuity diameter distribution) is often estimated from trace length measurements (Kulatilake and Wu, 1984; Mauldon, 1998; Zhang and Einstein, 1998, 2000; Li et al., 2014; Zhu et al., 2014). Information on discontinuities has traditionally been difficult, slow, and often dangerous to obtain by direct measurement using a tape and geological compass (Barton et al., 1974; Franklin et al., 1988). Currently, non-contact measuring techniques, such as photogrammetry and Light Detection and Ranging (LIDAR), provide alternative approaches to in situ measurement and allow discontinuities to be measured from photographs and 3D point clouds of rock mass exposures. These non-contact measuring techniques tremendously improve conventional geologic mapping due to the ability to take measurements without direct access to the rock mass and time restrictions, as well as to provide objective records of rock masses.

The two-dimensional image processing method has been used to extract discontinuity traces according to changes of pixel intensities (Crosta, 1997; Reid and Harrison, 2000; Hadjigeorgiou et al., 2003; Lemy and Hadjigeorgiou, 2003). However, the image processing method shows strong dependence on rock textures, illumination conditions, and threshold settings, often resulting in meaningless segments or excessive fragmentation (Ferrero et al., 2009). In addition, the use of the general-purpose image processing method has tended to show two other shortcomings: simultaneous highlighting of shadows and surface markings on the intact rock, and images acquired through uncalibrated cameras suffer from projective distortion and lens distortion that are difficult to rectify.

In recent years, many researchers have been working on the extraction of discontinuity traces from 3D surface models (Roncella et al., 2005; Gigli and Casagli, 2011), i.e., high-resolution 3D point clouds of rock mass surfaces. The photogrammetry technique is capable of obtaining 3D point clouds from pairs of 2D images. LiDAR technology is another solution to obtaining 3D point clouds. The pros and cons of both techniques have been discussed by many authors (Roncella et al., 2005; Potsch et al., 2005). Two main methods can be used to detect traces using a 3D surface model. First, discontinuity traces can be obtained as intersection lines between the fitting planes of rock mass surfaces (Slob et al., 2007; Otoo et al., 2011; Gigli and Casagli, 2011). However, the result is highly dependent on the accuracy of the fitting planes, which is further dependent on the segmentation accuracy of the rock mass surface. Second, traces can be detected based on the principal curvatures of the vertices on the digital surface model (DSM) of the rock mass (Umili et al., 2013).

Automated discontinuity trace mapping is an emerging method because discontinuity surfaces are irregular in shape, occur at any

* Corresponding author.
*E-mail address:* zhuhehua@tongji.edu.cn (H. Zhu).

http://dx.doi.org/10.1016/j.cageo.2015.12.010
0098-3004/

orientation, and contain variable amounts of small-scale roughness and large scale undulation (Vöge et al., 2013). This study is motivated by the following difficulties in automated discontinuity trace mapping: (1) feature point detection from 3D point clouds is noise sensitive (feature points are the vertices at the intersections of rock mass surfaces); (2) automated trace detection is prone interruption by uneven rock mass surfaces, resulting in fragmented discontinuity traces; (3) an automated identification process is difficult to achieve because of speculative selection of threshold values (Umili et al., 2013). This paper develops a robust and automated trace mapping method to extract discontinuity traces from the 3D surface model of natural outcrops or tunnel excavation faces. First, the Normal Tensor Voting Theory (Page et al., 2002) is utilized to reduce the interference of noisy data in trace feature point detection. Second, post-processing techniques are proposed to overcome the segmentation of extracted traces and to achieve smooth and continuous traces. Finally, the trace mapping process is streamlined without human intervention and is insensitive to the chosen thresholds.

This paper is organized as follows: an automated discontinuity trace mapping method is introduced in Section 2, sensitivity of the method is analyzed in Section 3, the method is then applied to trace mapping of a tunnel face under construction in Section 4, the application of the method is discussed in Section 5 and some conclusions are drawn in Section 6.

## 2. Methodology

The method for discontinuity trace mapping is divided into five steps: (1) trace feature point detection: vertices of the traces are identified and labeled as feature points; (2) trace feature point grouping: adjacent feature points are grouped for further processing; (3) trace segment growth: trace segments composed of a continuous chain of feature points are generated using a growth algorithm; (4) trace segment connection: segments that belong to a trace are connected; (5) redundant trace segment removal: feature points that do not lie in the main direction of the traces are removed to improve the quality of trace lines. The flow chart of the method is illustrated in Fig. 1.

### 2.1. Description of the datasets

Two 3D point cloud datasets are used in our study: the publicly available LiDAR data of a rock cut and the DSM of a rock tunnel excavation face. The first is used to make a comparison with previous studies and the second is for field application.

#### 2.1.1. Case study A

Case study A uses LiDAR data at the Rockbench open repository (Vöge et al., 2013). The complete 3D RAW data is available from www.3d-landslide.com/projects/discontinuity/ (Riquelme et al., 2014). The case is a rock cut located in Ouray, Colorado, USA (Fig. 2). This point cloud has 1,515,722 points and the resolution of the point is approximately 2 cm. The scanning took about 15 min using an Optech Ilris3D scanner.

#### 2.1.2. Case study B

Case study B is a highway rock tunnel situated in Yuexi County, Anhui Province, China. The tunnel was excavated using the drill and blast method. The total length of the tunnel is 7.548 km, and the lithology along the tunnel is primarily granite and gneiss. The 3D point cloud data were obtained using overlapping photographs (Roncella et al., 2005; Haneberg, 2008; Sturzenegger and Stead, 2009) to create 3D surfaces. Examples of commercial photogrammetry software for geological mapping include Sirovision, ShapeMetrix3D, 3DM Analyst, and Agisoft Photoscan. Fig. 3 (a) shows a picture of the tunnel excavation face and Fig. 3 (b) shows the reconstructed 3D point cloud with color after binocular 3D reconstruction.


**Fig. 2.** Image of a road cut slope from the Rockbench repository.

### 2.2. Automated trace mapping method

#### 2.2.1. Preprocessing of the dataset

The raw data that contain vegetation, unnecessary and sparse points will affect the precision of trace detection and also increase processing time. The first step is to remove these points to focus on the region of interest. As shown in Fig. 4, some holes (marked using red circles) are caused by the presence of vegetation and occlusions. In addition, the point cloud is noisy because of instrument errors, dust and dynamic disturbances in the open field (Slob, 2008). Therefore, the preprocessing of the point cloud is performed in the following steps: vegetation removal, point cloud resampling, noise reduction and triangulation.

First, the point cloud is resampled with a minimum distance of 3 cm to preserve rock mass geometry features and improve


**Fig. 1.** Flow chart of the proposed discontinuity trace mapping method.

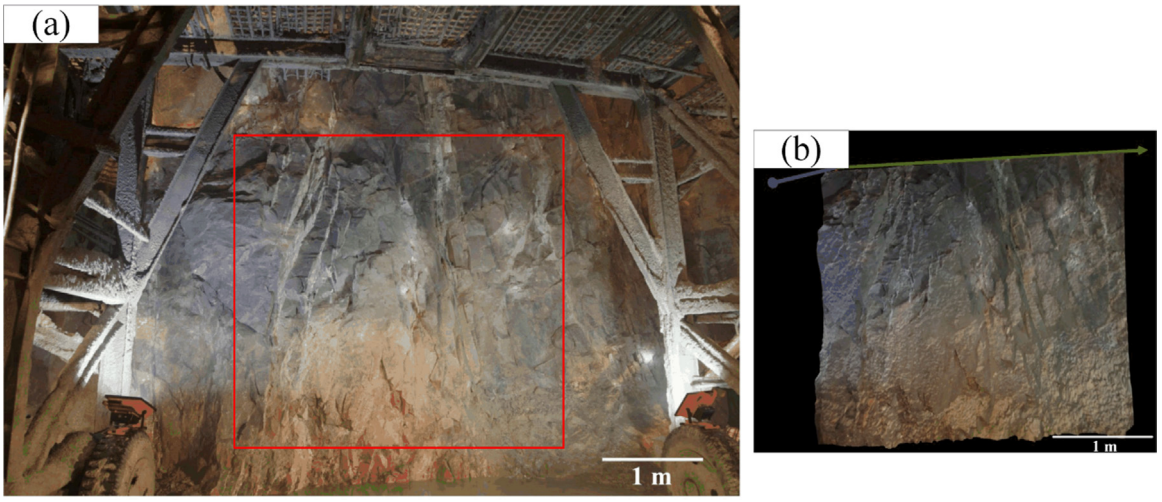


**Fig. 3.** Picture of the tunnel excavation face in the ZK21+697.9 mileage and its 3D point clouds with color within the red square. (For interpretation of the references to color in this figure legend, the reader is referred to the web version of this article.)

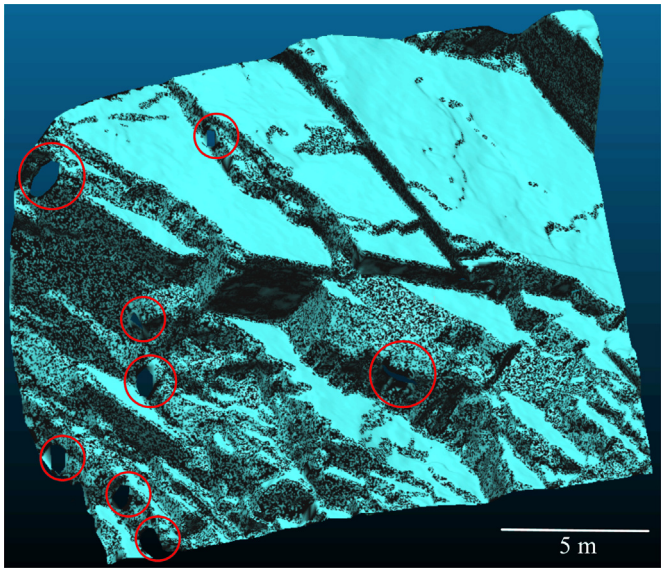


**Fig. 4.** Triangulation of a portion of the rock cut. (For interpretation of the references to color in this figure, the reader is referred to the web version of this article.)

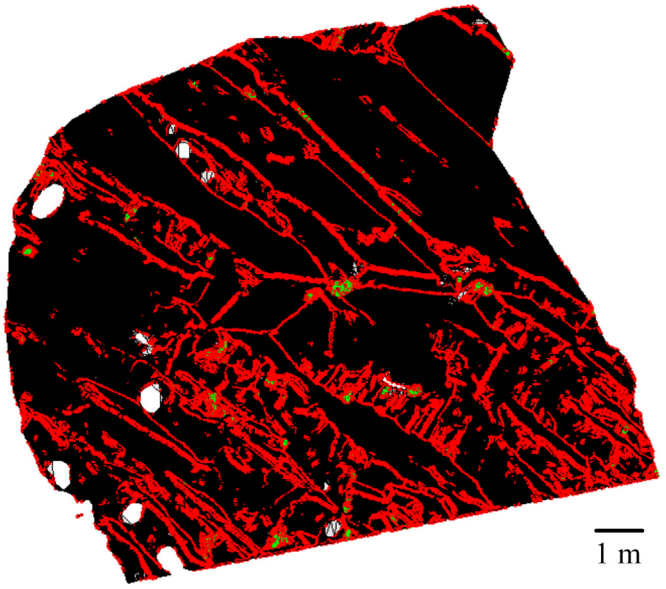


**Fig. 5.** Initial feature points: red represents sharp edge type points and green represents corner type points. (For interpretation of the references to color in this figure legend, the reader is referred to the web version of this article.)

processing speed. Then, the Moving Least Squares method (Alexa et al., 2003) is used to reduce the noise. Finally, a Delaunay triangulation algorithm is performed on the point cloud to obtain a 3D surface model of the rock mass slope using Halcon software (MVTec Software GmbH, 2012).

### 2.2.2. Trace feature point detection

*2.2.2.1. Normal tensor voting (NTV) method.* The traces on a triangulated mesh refer to the vertices on the edges and corners. An edge can be approximated based on the surface normal variation within a neighborhood because the surface normal has an abrupt change across edges (Sun et al., 2002). A robust detection can be achieved by a scheme called normal voting, which was extended from tensor voting. The voting scheme can be simply considered as the eigenvalue analysis of a set of surface normals (Medioni et al., 2000). The NTV method can handle sharp features and show robustness to noisy data.

A digital surface model (subsequently called DSM) is a triangulated point cloud that approximates the true surface. Given a triangular mesh composed of triangles $M = (V, E, F)$, $V = \{v_1, v_2, \cdots, v_n\}$ denotes a set of vertices, $E$ denotes a set of edges connecting two points belonging to the same triangle, and $F = \{f_1, f_2, \cdots, f_m\}$ denotes a set of faces, which are described by indices of the vertices. Each vertex $v_i \in V$ is represented using Cartesian coordinates, denoted by $v_i = (v_{ix}, v_{iy}, v_{iz})$.

The initial feature vertices can be extracted and classified based on the NTV. The NTV of a vertex is defined by

$$T_v = \sum_{f_i \in N_f(v)} \mu_{f_i} n_{f_i} n_{f_i}^T \tag{1}$$

where $n_{f_i} = (a, b, c)^T$ is the unit normal vector of triangle $f_i$, $N_f(v)$ is the face index of one-ring neighbors of $v_i$ and $\mu_{f_i}$ is a weight given by Kim et al. (2009)

$$\mu_{f_i} = \frac{A(f_i)}{A_{max}} \cdot \exp\left(-\frac{\|c_{f_i} - v\|}{\sigma/3}\right) \tag{2}$$

In the above equation, $A(f_i)$ is the area of triangle $f_i$, $A_{max}$ is the maximum area of $A(f_i)$, $c_{f_i}$ is the barycenter of triangle $f_i$, and $\sigma$ is the edge length of a cube that defines the neighboring space of each vertex.

$T_v$ can be represented as:

$$T_v' = \lambda_1 e_1 e_1^T + \lambda_2 e_2 e_2^T + \lambda_3 e_3 e_3^T \tag{3}$$

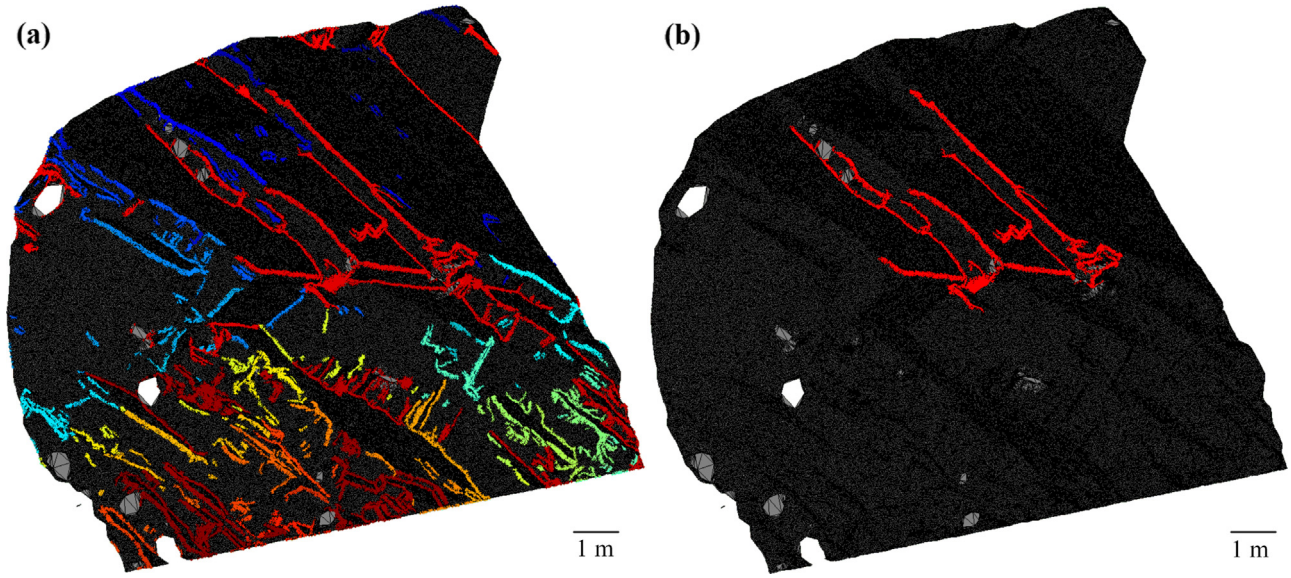


**Fig. 6.** Feature point grouping result. Each group is represented by one color in (a). In (b), points of multiple traces are grouped in the same point set and need to be subdivided.

where $\lambda_1 \geq \lambda_2 \geq \lambda_3 \geq 0$ are its eigenvalues and $e_1$, $e_2$, and $e_3$ are the corresponding unit eigenvectors.

According to the eigenvalues (Kim et al., 2009), vertices can be classified into face type, sharp edge type, and corner type by the following rules:

- Face type: $\lambda_1$ is dominant, and $\lambda_2$, $\lambda_3$ are close to 0.
- Sharp edge type: $\lambda_1$, $\lambda_2$ are dominant, and $\lambda_3$ is close to 0.
- Corner type: $\lambda_1$, $\lambda_2$ and $\lambda_3$ are approximately equal.

Both sharp edge type and corner type vertices are called feature vertices.

*2.2.2.2. Detecting the initial feature vertices.* Two thresholds, $\alpha$ and $\beta$, are defined to control the detection accuracy of corner type points and edge type points, respectively. Both thresholds $\alpha$ and $\beta$ can be determined by visual evaluation of the number of detected edge type and corner type vertices. Threshold $\alpha$ should be sufficiently large to avoid extracting many false corners. Threshold $\beta$ is a fine-tuning parameter around a value for finding a tradeoff between detecting weak features and an extra number of noisy vertices (Wang et al., 2012). The pseudo-code of detecting initial feature vertices is listed in Algorithm 1. Fig. 5 shows the result of the initial feature point detection.

**Algorithm 1.** Detect the initial feature vertices.

**Input:** $n$ is the number of vertex, $\alpha$ and $\beta$ are user-defined thresholds.

**Output:** {*FaceV*}, {*EdgeV*}, and {*CornerV*} are the indices of face, edge and corner type vertices, respectively.

1. Arrange the eigenvalues in descending order: $\lambda_1 \geq \lambda_2 \geq \lambda_3$
2. **for** $i \leftarrow 1$ to $n$ **do**
3. **if** $\lambda_3 \leq \alpha$ **then**
4. **if** $\lambda_2 \leq \beta$
5. $\{FaceV\} \leftarrow FaceV_i$
6. **else**
7. $\{EdgeV\} \leftarrow EdgeV_i$
8. **end if**
9. **else**
10. $\{CornerV\} \leftarrow CornerV_i$
11. **end if**
12. **end for**

*2.2.3. Trace feature point grouping*

Through the above analysis, all feature points constituting traces are obtained. However, the feature points representing different traces are stored in one point set. Adjacent feature points are grouped in this step for subsequent analysis.

The feature points can be assigned to the same group if the following two conditions are met: (1) the feature points share the same edge; (2) the angle between the normal vectors of the feature points is less than a threshold $\theta_1$. The threshold $\theta_1$ can be simply set to approximately 60° according to our data testing. The pseudo-code of the trace feature points grouping is listed in Algorithm 2.

**Algorithm 2.** Trace feature point grouping.

**Input:** {*EdgeV*} and {*CornerV*} are the indices of edge and corner type vertices, respectively, and $\theta_1$ is the angle threshold.

**Output:** $\{G_p\}$ is the set storing grouped feature points.

1. $\{V_{Fea}\} \leftarrow \{EdgeV\} \cup \{CornerV\}$
2. $j \leftarrow 1$ // $j$ is the searched group number
3. Randomly choose a feature point $V$ in the set $\{V_{Fea}\}$
4. Find the immediate neighboring point of $V$, represented as $V_N$ ($N=1,2,3\ldots$)
5. Compute the angle $\theta_{VV_N}$ of $V$ and the normal vector of $V_N$ ($N=1,2,3\ldots$)
6. Find the feature point in $V_N$ which meets the condition $\theta_{VV_N} < \theta_1$, represented as $\{V_{cur}\}$ //$\{V_{cur}\}$ is the set storing the new growing feature points
7. Merge the feature points in $\{V_{cur}\}$ into $\{G_p(j)\}$
8. For each feature point $V_c$ in $\{V_{cur}\}$, $V \leftarrow V_c$, repeat line 4 to line 7 until no feature point in $\{V_{cur}\}$ meets the condition $\theta_{VV_N} < \theta_1$
9. Exclude all of the feature points $\{G_p(j)\}$ from $\{V_{Fea}\}$: $\{V_{Fea}\} \leftarrow \{V_{Fea}\} - \{G_p(j)\}$
10. Start to find next group, $j \leftarrow j+1$
11. Repeat line 3 to line 10 until all feature points are processed

Through the above procedures, the feature points are divided into different groups and each group is composed of adjacent feature points. Fig. 6(a) shows the grouping result. It can be seen from Fig. 6(b) that feature points of multiple traces are grouped in the same point set. These feature points need to be subdivided. In addition, one trace may also be separated to several groups that

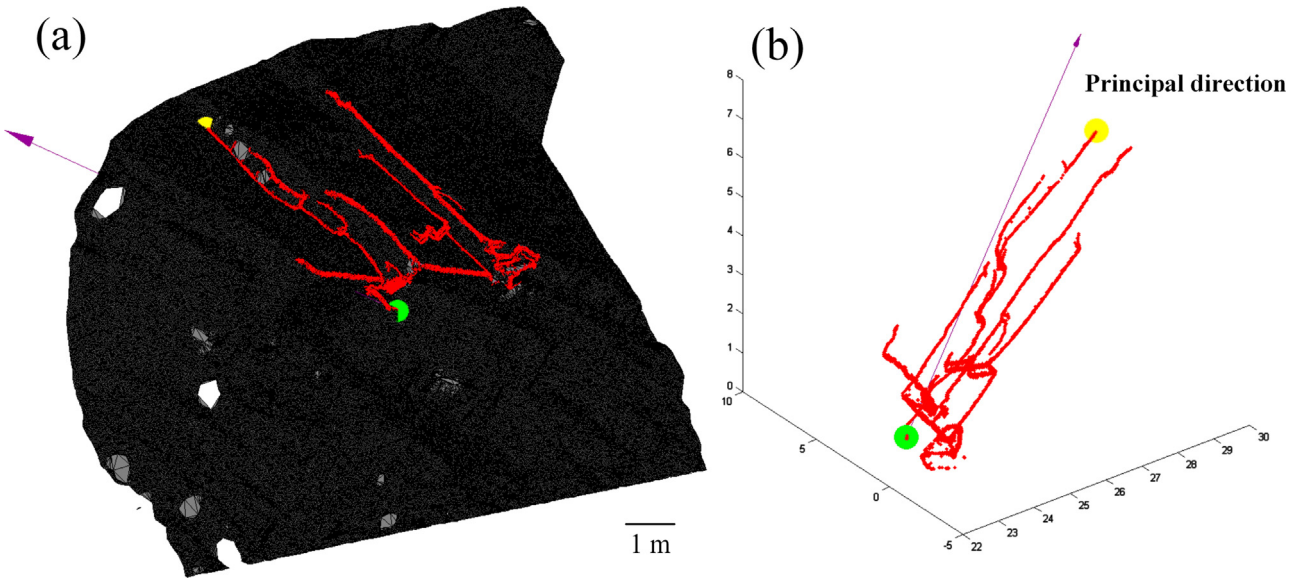


**Fig. 7.** The principal direction of the group. The seed point is plotted in yellow, and the randomly selected point is plotted in green. (For interpretation of the references to color in this figure legend, the reader is referred to the web version of this article.)

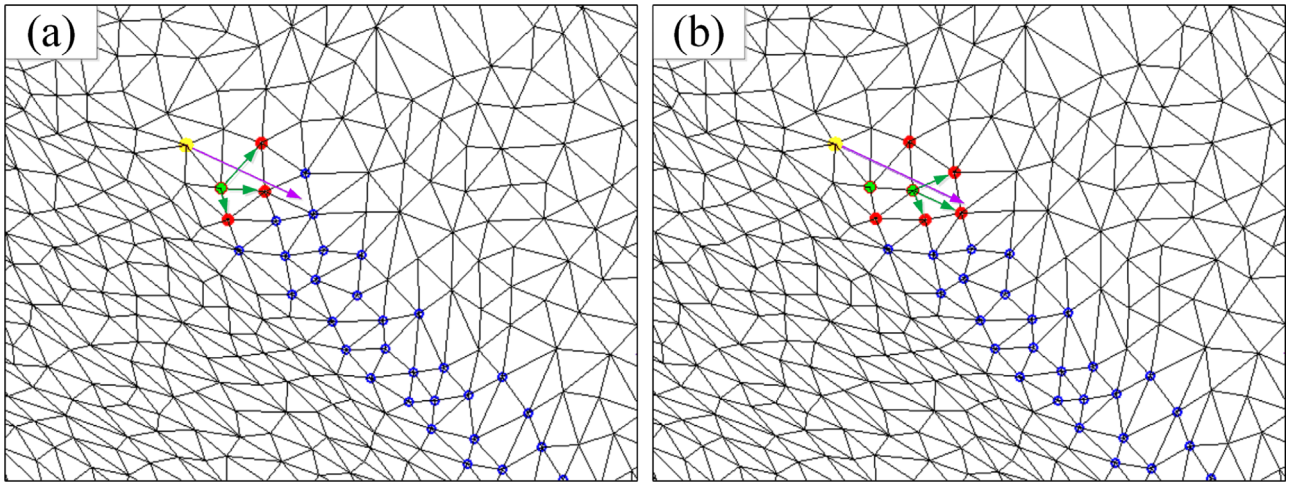


**Fig. 8.** The growing process of feature points. The seed point is plotted in yellow. The growth point is plotted in green. The principal direction is represented with a purple arrow. (For interpretation of the references to color in this figure legend, the reader is referred to the web version of this article.)

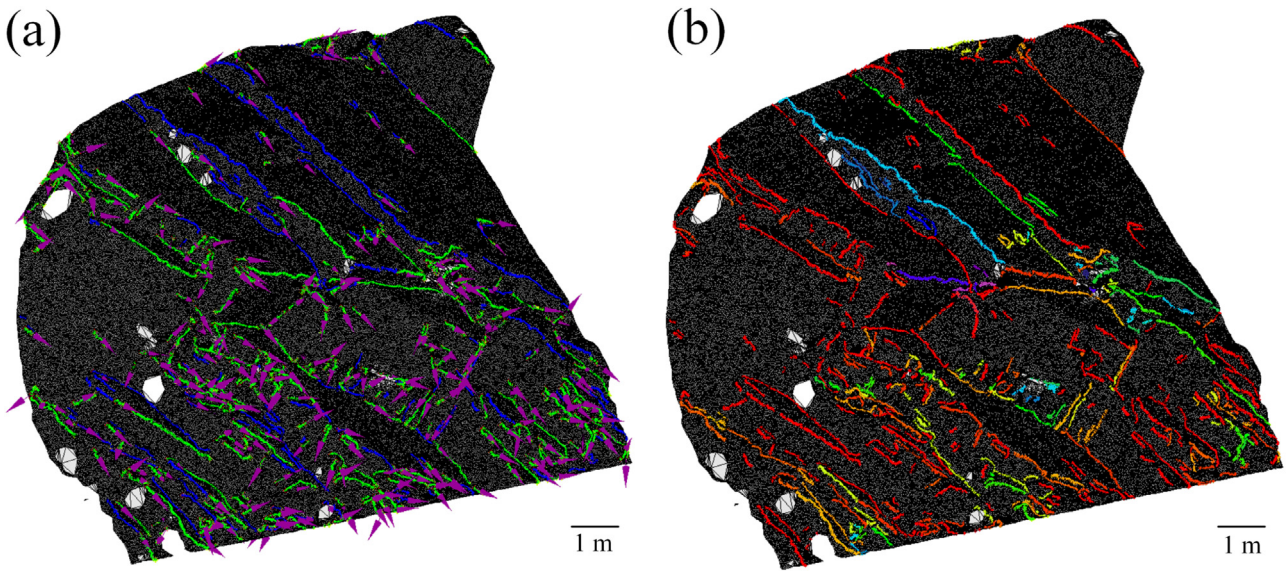


**Fig. 9.** Trace segment connection: in (a), the start segment is plotted in green, the growth segment is plotted in blue, and the principal direction of the current segment is represented with a purple arrow. The trace segment connection result is shown in (b) and each trace is represented using a color. (For interpretation of the references to color in this figure legend, the reader is referred to the web version of this article.)

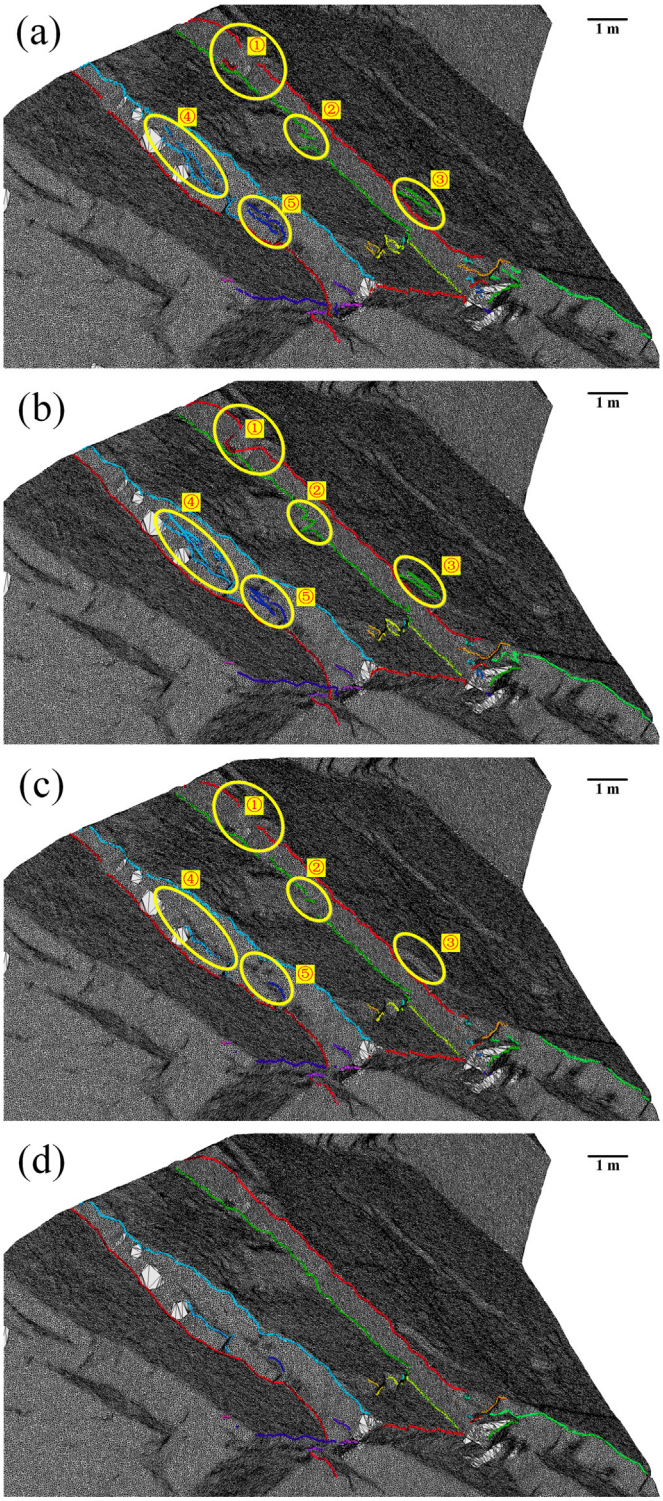


**Fig. 10.** Redundant trace segment removal.

need to be connected. In the following steps, trace segments composed of a continuous chain of feature points are first generated using the growth algorithm in Section 2.2.4, and then connected to form continuous traces, as in Section 2.2.5.

### 2.2.4. Trace segment growth

The growth algorithm is based on the simple idea that a trace can be stretched along a linear trend defined by its feature points. It requires an iterative procedure to search for segments of a trace

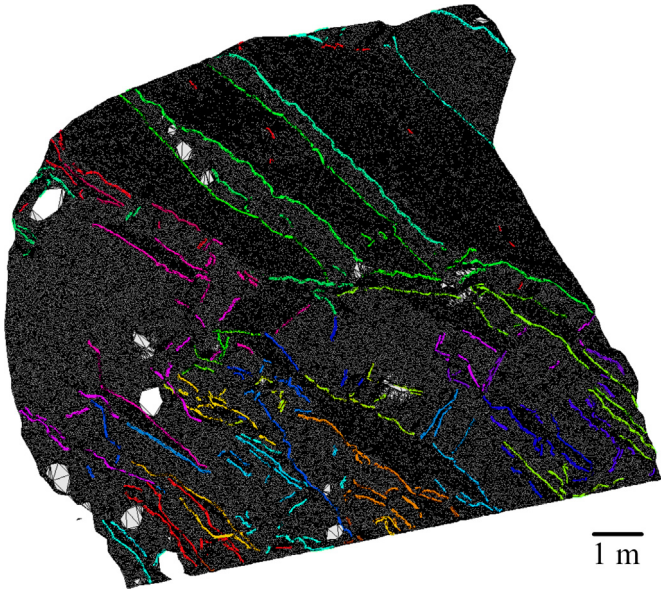


**Fig. 11.** Final trace mapping results of the entire area.

because discontinuity surfaces are irregular and uneven in shape, and is unable to accomplish a complete growth only once.

*2.2.4.1. Principal direction computation.* The method we used to compute the average orientation of a point set is called principal component analysis (PCA) (Person, 1901). PCA is performed by first calculating the covariance matrix:

$$M_p = \frac{1}{n}\sum_{i=1}^{n}(v_i - c_0)(v_i - c_0)^T \tag{4}$$

where $v_i$ is the $i^{th}$ vertex, $n$ is the number of points and $c_0$ is the centroid of the point cloud calculated as the arithmetic mean of the coordinates. Because $M_p$ is a symmetric and positive matrix, it can be decomposed by means of eigenvalue decomposition.

The covariance matrix can be composed as follows:

$$M_p' = \sum_{i=1}^{3} k_i e_i e_i^T \tag{5}$$

where $k_1 \geq k_2 \geq k_3$ are its eigenvalues. The principal direction $\vec{P}$ is the first eigenvector $e_1$ of covariance matrix $M_p$ (Dimitrov, 2009).

To ensure a continuous growth, the calculation of the computational direction $\vec{P_c}$ should reflect the overall trend of the point set. In addition, the computational direction $\vec{P_c}$ should also take the local bending of traces into account. Our strategy is that when the number of the points in $\{T_V\}$ is less than 10 at the beginning of the segment growth, taking the principal direction $\vec{P}$ as the computational direction to overcome the local bending of traces. When the number of the points in $\{T_V\}$ exceeds 10, the direction $\vec{P_c}$ of the nearest five points in the $\{T_V\}$ is computed by PCA to reflect the direction variation near the growing points and extend the trace as long as possible.

*2.2.4.2. Seed point selection.* The selection of the seed point should avoid the growing direction beginning from a branch that generates traces that are too short. The strategy here is projecting all points orthogonally to the principal direction $\vec{P}$ and selecting the farthest point away from the randomly chosen point as the seed point. As shown in Fig. 7, the seed point (plotted in yellow) is the farthest point in the principal direction $\vec{P}$ of the randomly selected point (plotted in green). This strategy ensures the seed point is selected from the end of the longest trace of current analyzing feature points.

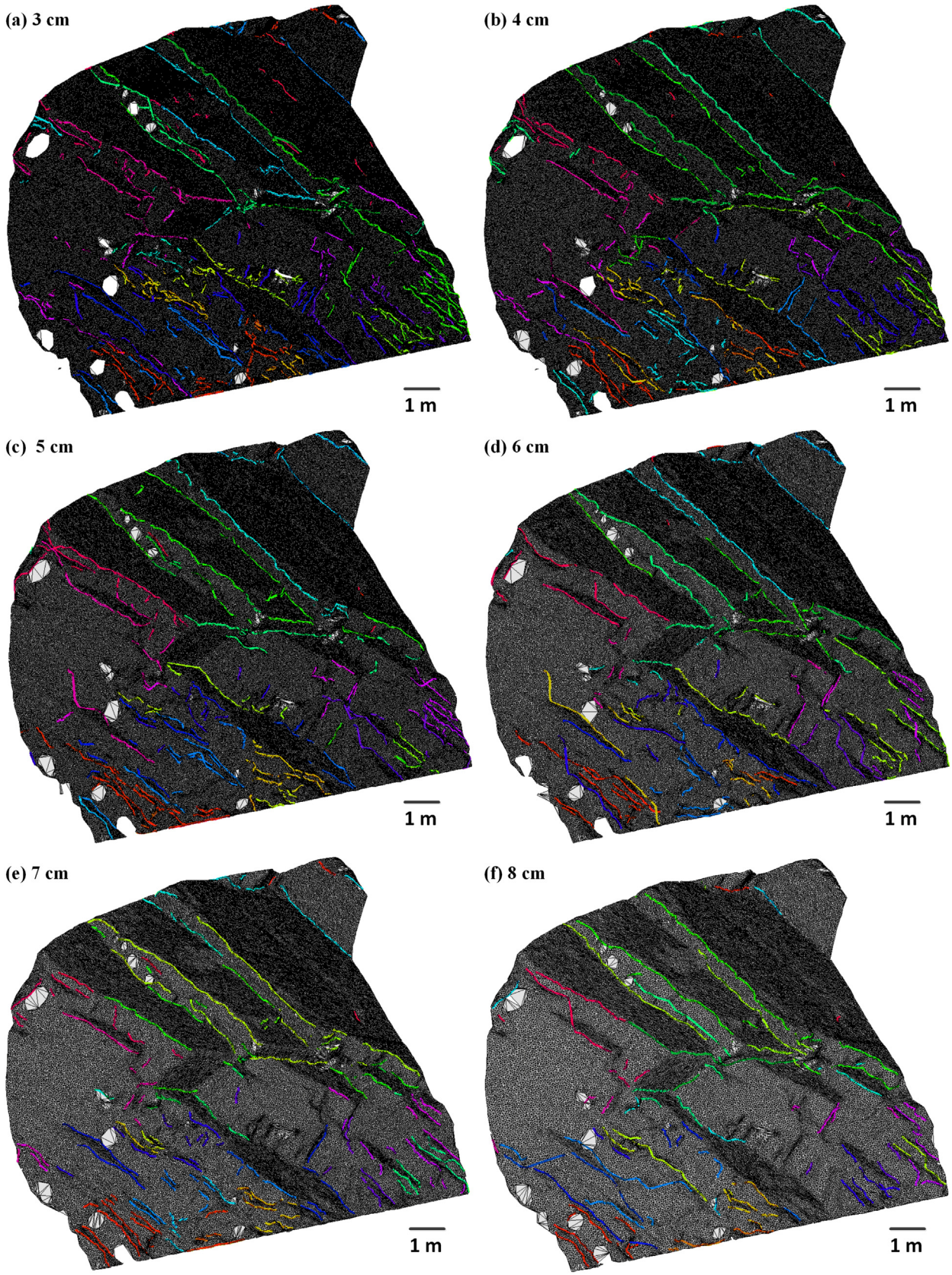


**Fig. 12.** Trace mapping results using triangular mesh sizes of 3 cm, 4 cm, 5 cm, 6 cm, 7 cm, and 8 cm.

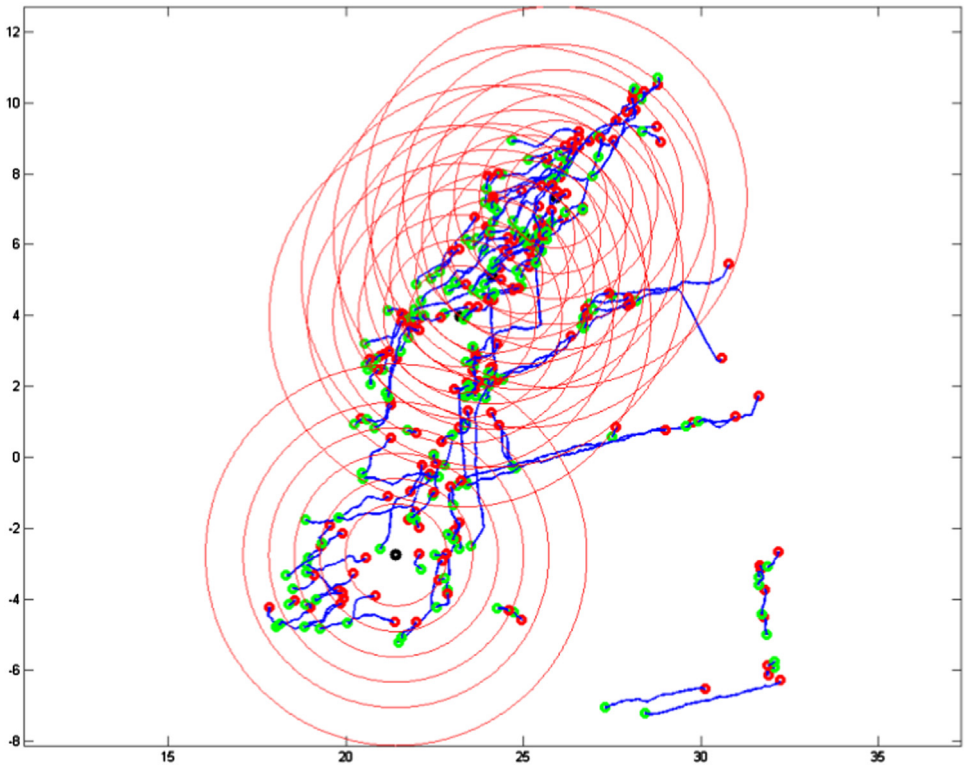

**Fig. 13.** Example of six circular windows in different locations.

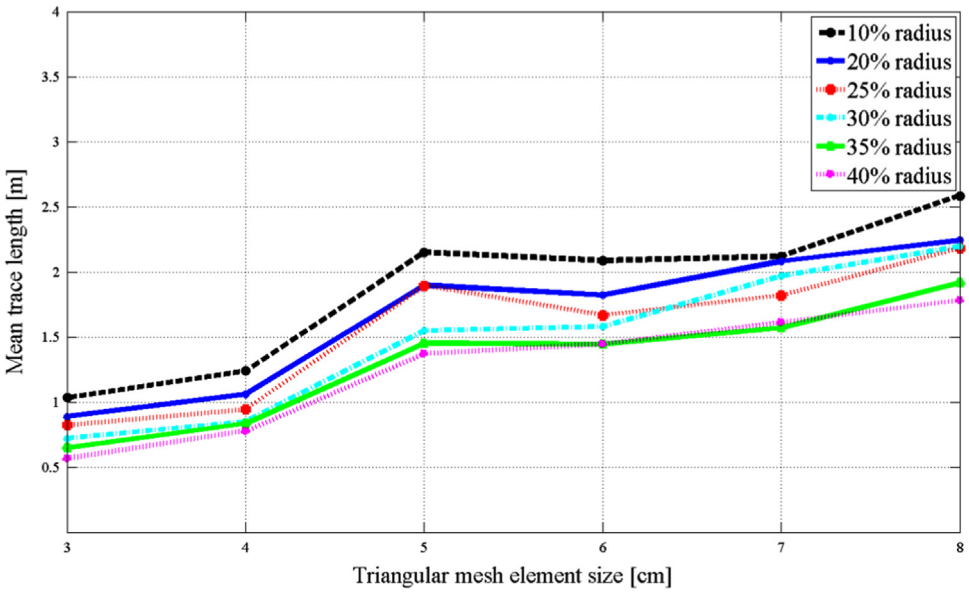


**Fig. 14.** Mean trace length with different triangular mesh sizes.

*2.2.4.3. Growing criteria.* The feature point can grow if it satisfies one of the following two conditions:

$$\min\left(\theta\left(\vec{P_c}, \vec{X}_{VV_N}\right)\right) \le \theta_2 \tag{6}$$

$$num(V_N) = 1 \tag{7}$$

where $\theta(\vec{P_c}, \vec{X}_{VV_N})$ is the angle between the computational direction $\vec{P_c}$, in which the vector $\vec{X}_{VV_N}$ started from the current feature point $V$ and ended at the neighboring feature point $V_N$, $\theta_2$ is a user-defined threshold angle, and num$(V_N)$ is the number of neighboring feature points $V_N$.

Eq. (7) is used to prevent odd shapes of triangular facets at the corner that will cause the interruption of growth.

As shown in Fig. 8(a), the seed point is plotted in yellow and the current growth point is plotted in green. For its three neighboring feature points (plotted in red), the points that satisfy Eq. (6) are merged. These steps are repeated until no neighboring feature points can be found (Fig. 8(b)). Finally, grow will occur in the opposite direction to include all of the trace feature points. The pseudo-code for the trace segment growth is listed as follows:

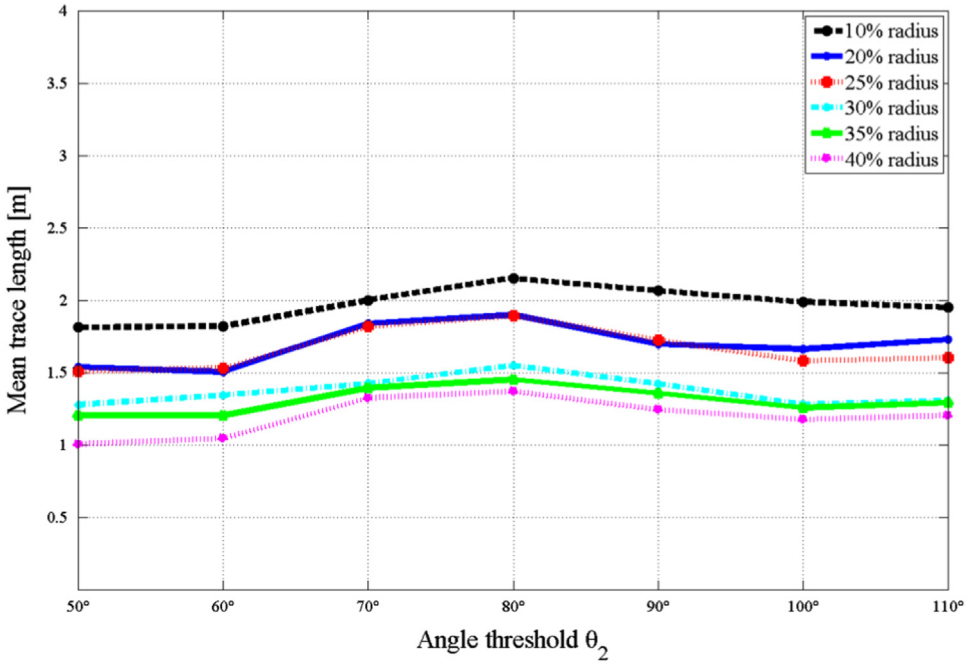


**Fig. 15.** Mean trace length with different angle threshold $\theta_2$ values.

**Algorithm 3.** Trace segment growth

**Input**: $\{G_p\}$ is the set storing grouped feature points obtained in Section 2.2.3, and $\theta_2$ is an angle threshold.

**Output**: $\{Seg\}$ is the set storing trace segments.

1. Calculate the number of groups $m$ in $\{G_p\}$
2. $index \leftarrow 0$ // $index$ is the number of current detected trace segments
3. **for** $j \leftarrow 1$ to $m$ **do**
4. Select a seed point $V_s$ as described in Section 2.2.4.2
5. $\{T_V\} \leftarrow V_s$ // $\{T_V\}$ is the set storing the growing feature points.
6. Choose the last point in $\{T_V\}$ as current feature point $V$
7. Find the neighboring features points $V_N$ of $V$
8. Compute the angles $\theta(\vec{P_c}, \vec{X}_{VV_N})$ between the principal direction $\vec{P_c}$ and the vectors $\vec{X}_{VV_N}$
9. Add the new growing point to the end of $\{T_V\}$ if it satisfies Eq. (6) or Eq. (7)
10. Repeat Line 6 to Line 9 until no more points are added to $\{T_V\}$
11. Grown in the opposite direction.
12. $index \leftarrow index + 1$
13. Save the current segment: $\{Seg(index)\} \leftarrow \{T_V\}$
14. **end for**

### 2.2.5. Trace segment connection

The above procedure generates segments that actually belong to one trace. It is necessary to connect them together to produce a continuous trace. The strategy in connecting trace segments is similar to the trace growing method, except that the growing objects are segments instead of feature vertices. Each trace segment is a list of vertices and can be described using $(X_{st}, Y_{st}, Z_{st}, X_{end}, Y_{end}, Z_{end}, l, m, n)$, where $(X_{st}, Y_{st}, Z_{st})$, $(X_{end}, Y_{end}, Z_{end})$, and $(l, m, n)$ are the starting point of the segment, end point of the segment and principal directions of the segment, respectively. The connection criteria are characterized by the angle threshold $\theta_3$ and the distance threshold $d$ between two edge segments.

Fig. 9(a) shows the connection of segments and Fig. 9(b) shows the connected traces. Each trace is represented using a different color. It can be seen from Fig. 9(b) that trace fragmentation has been reduced.

### 2.2.6. Redundant trace segment removal

Discontinuity surfaces are irregular in shape and contain variable amounts of small-scale roughness and large-scale undulations. As a result, the directions at the end of trace segments vary dramatically with regards to the principal direction, as shown in regions ① and ② in Fig. 10(a). These two breaks cannot be connected because they do not meet the trace segment connection criteria. However, redundant trace segments may be generated by the segment growth and connection procedure, as shown in regions ③, ④, and ⑤ in Fig. 10(a). Trace smoothing means that trace segments are connected as a continuous and linear curve. Complex polygons will be produced if a trace smoothing or fitting method (e.g., Garcia, 2010, 2011) is immediately applied, as shown in regions ③, ④, and ⑤ in Fig. 10(b). The redundant trace segments are approximately parallel to each other with a small distance. Therefore, they can be removed by setting up an angle threshold $\theta_4$. According to testing experience, the angle threshold $\theta_4$ can be simply set to 60°. If the angle between the trace segment and the principal direction is greater than $\theta_4$, the trace segment can be removed to eliminate fitting disturbance caused by redundant traces. Fig. 10(c) shows that redundant traces are eliminated. Fig. 10(d) shows the trace smoothing after redundant trace segments have been removed. The traces are smoothly connected in the concave and convex regions of the discontinuities. Fig. 11 shows the final trace mapping result of the entire area.

## 3. Results for case study A: sensitivity analysis and calibration

The effects of triangular mesh element size, the angle threshold $\theta_2$ in the trace segment growth step (described in Section 2.2.4), the angle threshold $\theta_3$ and distance threshold $d$ (described in Section 2.2.5) in the trace segment connection step are important parameters of the automated trace mapping method. The sensitivity of the four parameters is investigated in this section.

### 3.1. Effect of triangular mesh element size

The raw point cloud is resampled using triangular mesh sizes 3 cm, 4 cm, 5 cm, 6 cm, 7 cm, and 8 cm. Traces of the six DSMs are identified through the above five steps and results are shown in Fig. 12. It can be observed that the amount of small discontinuity traces reflecting uneven discontinuity surfaces decreases with increasing triangular element mesh size.

The mean trace length is used as a metric to evaluate the influence of triangular mesh size. The mean trace length is calculated using the circular window sampling method (Zhang and Einstein, 1998). An automated trace sampling procedure (Umili et al., 2013) is employed. Traces are projected on the sample plane ($x$–$y$ plane) orthogonally. Then, the centers of six circular windows with different radii are placed in locations with dense traces (Fig. 13). The radii are 10%, 20%, 25%, 30%, 35%, and 40% of the sampling area. The mean trace length is estimated using the following equation (Zhang and Einstein, 1998):

$$\hat{\mu} = \frac{\pi(\hat{N} + \widehat{N_0} - \widehat{N_2})}{2(\hat{N} - \widehat{N_0} + \widehat{N_2})}c \tag{8}$$

where $N_0$ is the number of traces with both ends censored, $N_1$ is the number of traces with one end censored and one end observable, $N_2$ is the number of traces with both ends observable, and $c$ is the radius of the window.

The mean trace length is shown in Fig. 14. The overall trend is that the mean trace length initially increases, then stabilizes and finally increases again as the triangular mesh element size increases. When the triangular mesh size is 3 cm, many small discontinuity traces in the concavo–convex regions are generated. Some of these small traces are part of continuous traces that could not be connected due to obvious directional variation in the uneven regions. With increasing triangular element mesh size, the

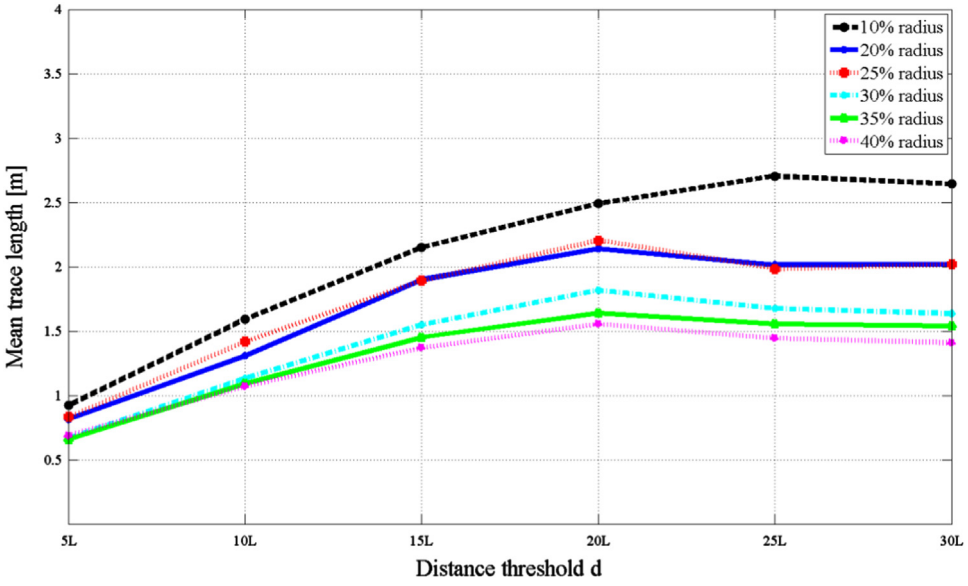


**Fig. 16.** Mean trace length calculated with different distance threshold $d$ values.

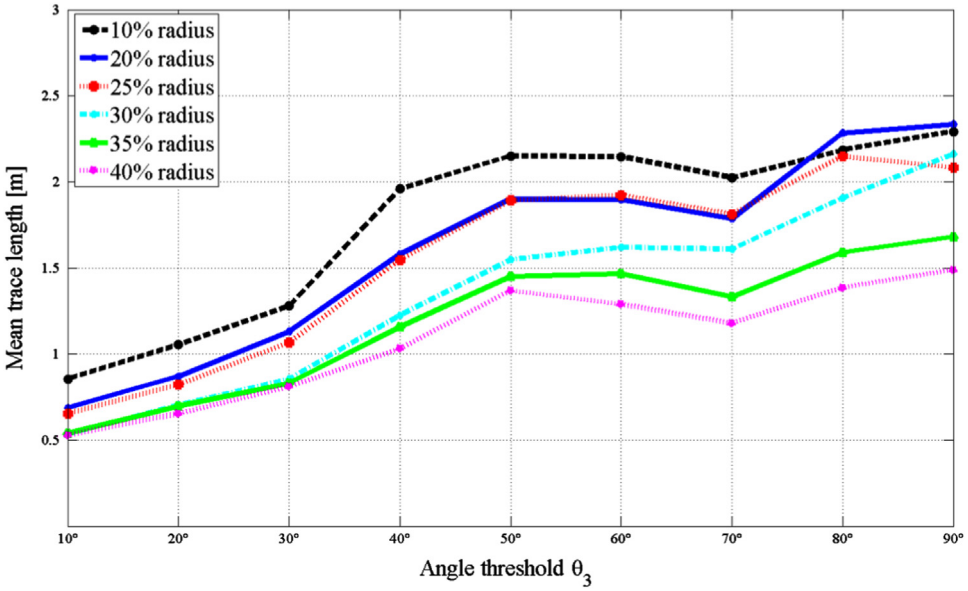


**Fig. 17.** Mean trace length with the angle threshold $\theta_3$.

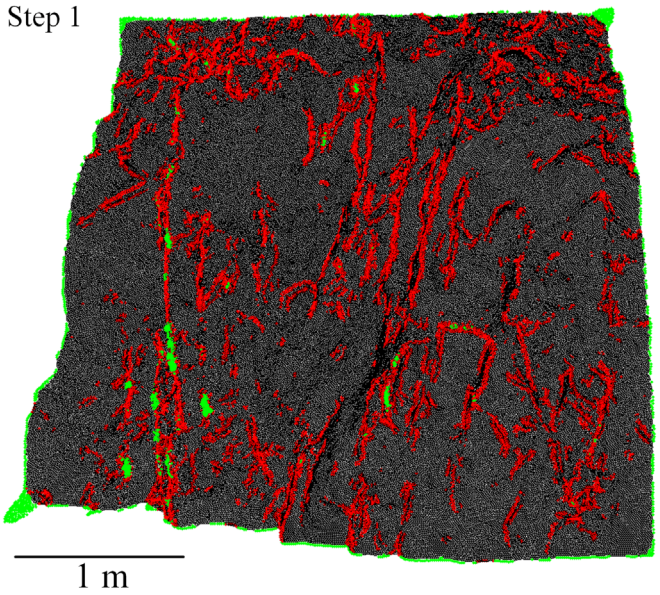


**Fig. 18.** Initial feature points obtained using normal tensor voting: red represents sharp edge type points and green represents corner type points. (For interpretation of the references to color in this figure legend, the reader is referred to the web version of this article.)

DSM becomes smoother and the ridge-valley lines reflecting the uneven surfaces of the discontinuity are diminished gradually. A portion of these small traces is connected to continuous traces. Therefore, when the triangular mesh size is between 3 cm and 5 cm, the mean trace length grows rapidly. When the triangular mesh size is between 5 cm and 7 cm, the mean trace length tends to be stable as no more small traces are detected and connected. However, when the triangular mesh size exceeds 7 cm, some traces are wrongly connected, resulting in larger mean trace lengths. Therefore, the optimal triangular mesh element size for this case is between 5 cm and 6 cm.

### 3.2. Effect of the angle and distance thresholds

(1) The angle threshold $\theta_2$ in the trace segment growth step
The angle threshold $\theta_2$ uses seven values (50°, 60°, 70°, 80°, 90°, 100°, and 110°), while the triangular mesh element size remains at 5 cm, the angle threshold $\theta_3$ is 50° and the distance threshold $d$ is maintained at 15 times the mean triangular mesh element size. As shown in Fig. 15, the general trend is that the mean trace lengths increase slightly initially, then decrease with increasing $\theta_2$. In regions where discontinuity surfaces are irregular and uneven, the triangulation mesh is often distorted. When $\theta_2$ is between 50° and 70°, the growth algorithm tends to be

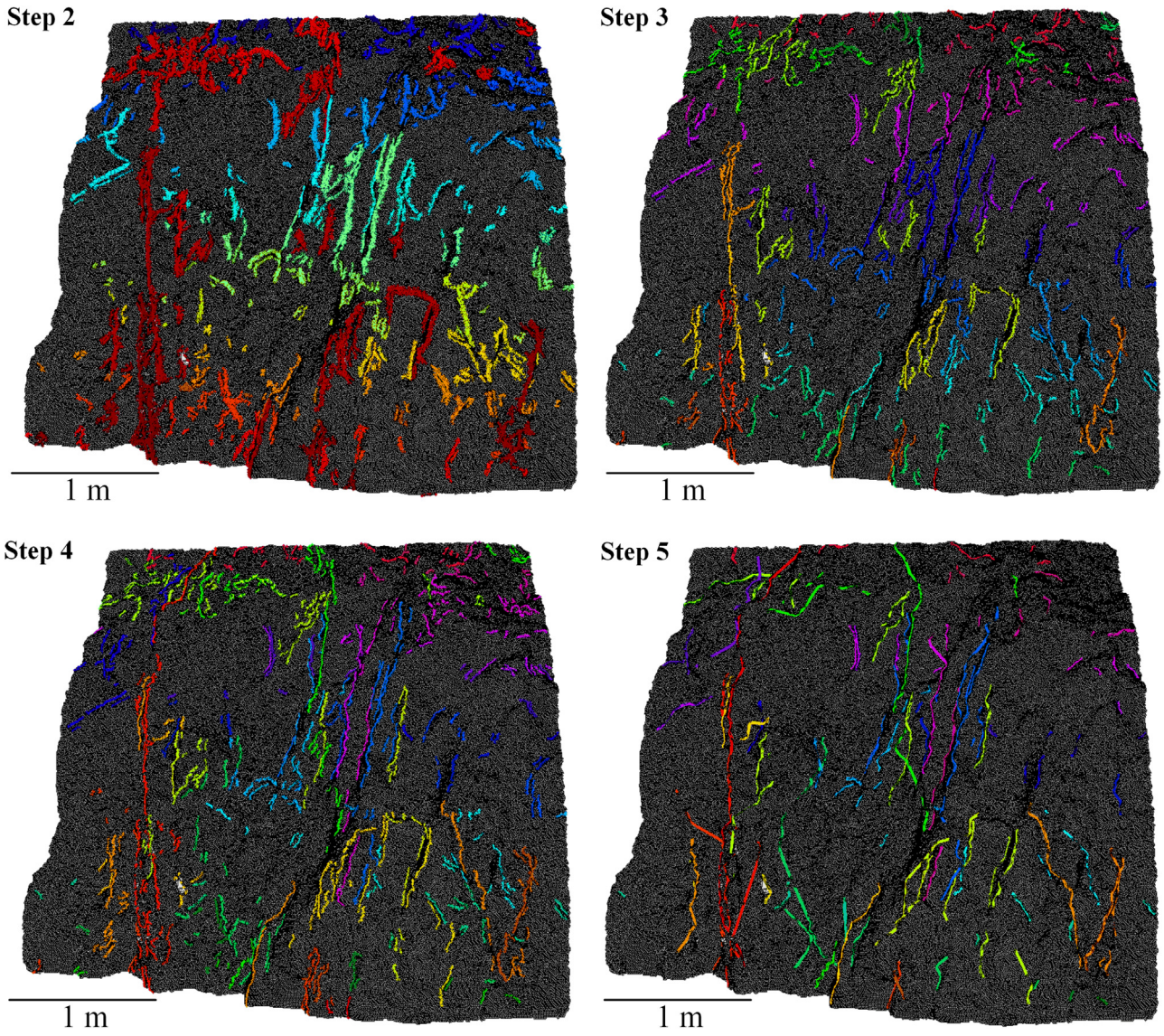


**Fig. 19.** Discontinuity traces produced by each post-processing step.

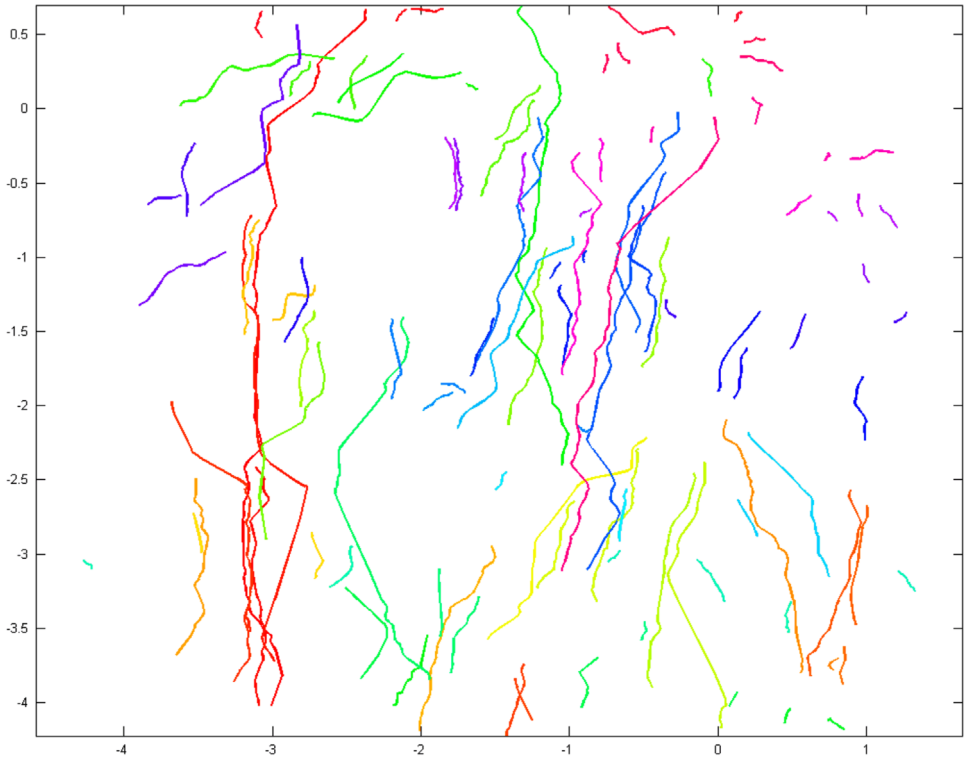


**Fig. 20.** Traces projected on the sampling plane.

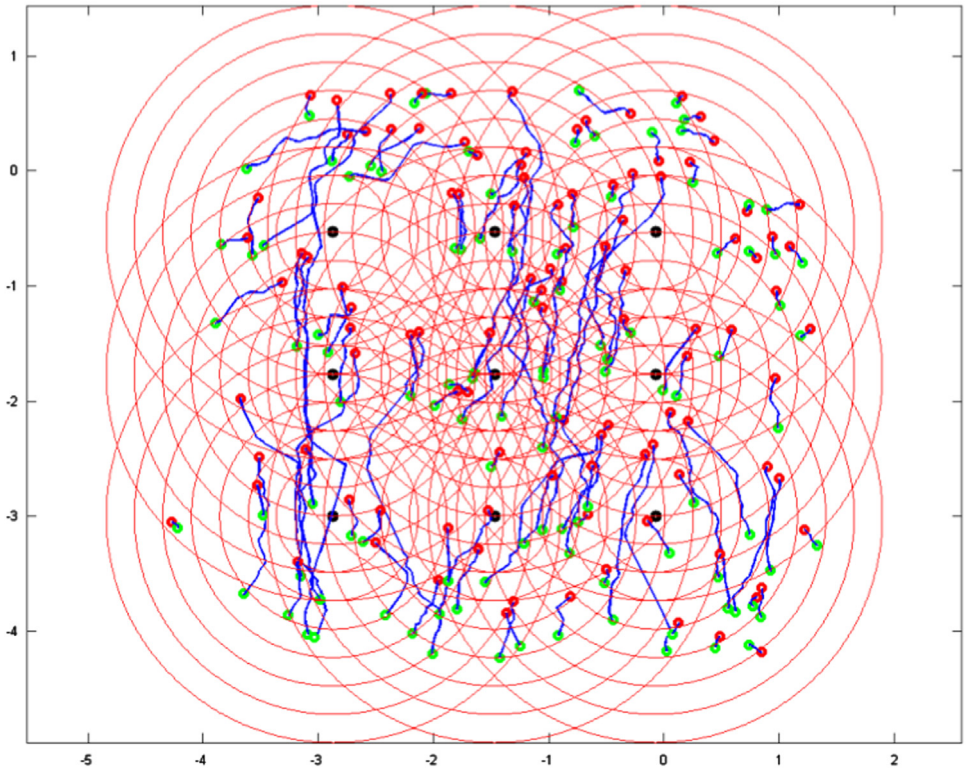


**Fig. 21.** Traces sampled using circular windows of seven radii at 9 locations.

interrupted prematurely. When $\theta_2$ is between 90° and 110°, trace segments that deviate from the straight line will be generated, and cannot be connected in the trace segment connection step. When $\theta_2$ is in between 70° and 90°, the mean trace length is relatively larger. Therefore, the optimal angle threshold $\theta_2$ in the trace segment growth step is between 70° and 90°.

(2) The angle threshold $\theta_3$ and the distance threshold $d$ in the trace segment connection step.

In this section, the triangular mesh element size is held constant 5 cm, $\theta_2$ is 80°, and $\theta_3$ is 50°. The distance threshold $d$ changes with six values (5 L, 10 L, 15 L, 20 L, 25 L, and 30 L, where L

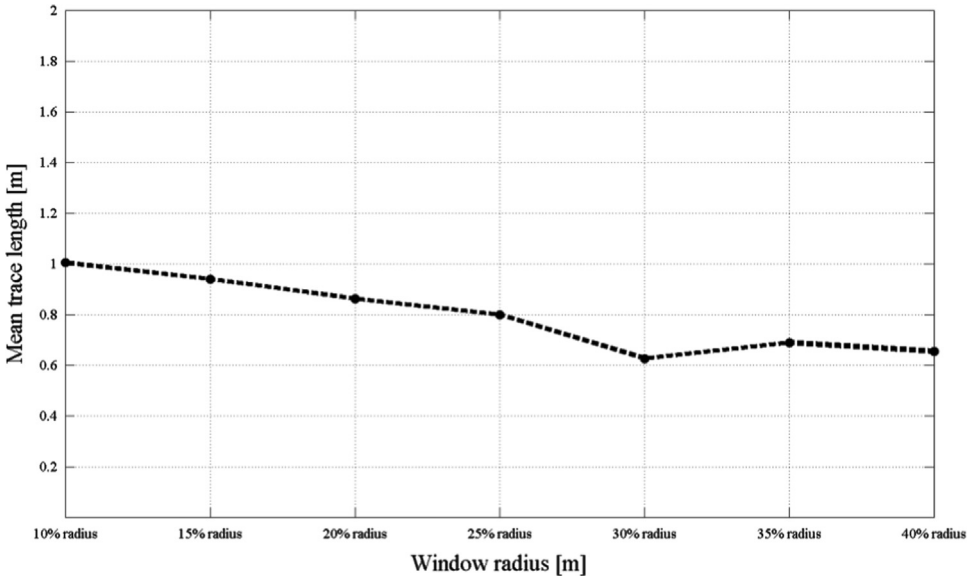


**Fig. 22.** Mean trace length with different sampling window radii.

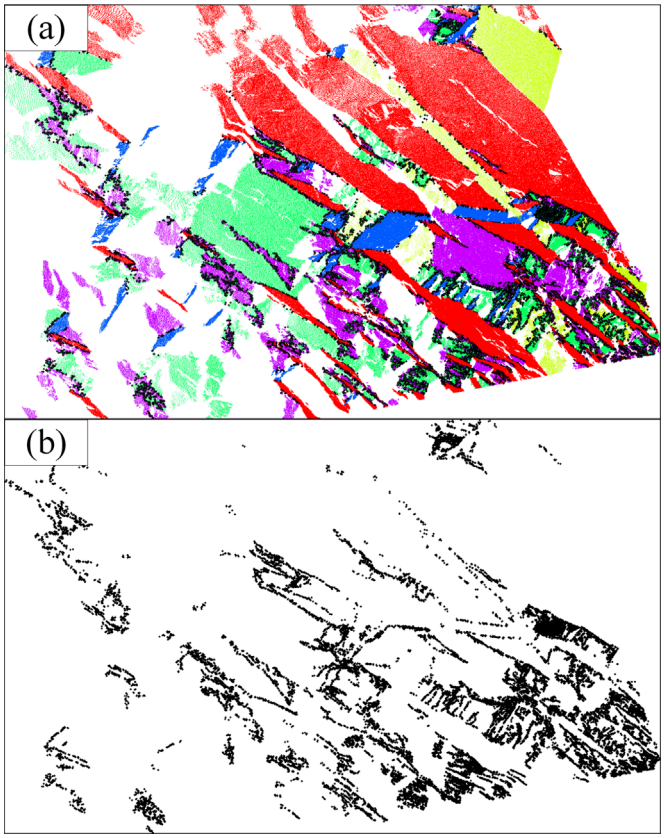


**Fig. 23.** Traces detected as intersection lines between the fitting planes of discontinuities and rock mass surfaces.

is the triangular mesh element size). As shown in Fig. 16, with increasing distance threshold $d$, the mean trace length increases continuously until it reaches a stable level. Therefore, the optimal distance threshold $d$ in the connecting algorithm should be specified at least 15 times that of the mean triangular mesh element size.

The angle threshold $\theta_3$ uses 9 values (10°, 20°, 30°, 40°, 50°, 60°, 70°, 80°, and 90°) while the triangular mesh element size is 5 cm, $\theta_2$ is 80° and the distance threshold $d$ is 15 times that of the mean triangular mesh element size. As shown in Fig. 17, the mean trace length increases sharply when $\theta_3$ increases from 10° to 50°. Then it stabilizes when $\theta_3$ ranges between 50° and 70°. However, it grows again when $\theta_3$ is in the interval between 70° and 90°. This is because segments near the main direction of the trace are connected constantly with the increasing of $\theta_3$, resulting in the increase in mean trace length. However, when $\theta_3$ is greater than 70°, segments can be wrongly connected. Therefore, the optimal angle threshold $\theta_3$ in the trace segment connection step could be set between 50° and 70°.

## 4. Results for case study B: a drill-and-blast highway tunnel

Initial feature vertices obtained using the NTV theory are shown in Fig. 18, and the results produced by each post-processing step are shown in Fig. 19. As shown in Fig. 19, small trace segments are connected and discontinuity traces become more continuous from step 2 to step 5.

Traces are projected to the sampling plane orthogonally (Fig. 20) and then sampled using seven concentric windows of different radii. The radii of the windows are 10%, 15%, 20%, 25%, 30%, 35%, and 40% of the sampling area, and the centers of the window are uniformly placed at nine locations, as shown in Fig. 21. Mean trace length is plotted in Fig. 22. The overall trend observed in the figure shows that the mean trace length decreases with the increasing of sampling window radius and stabilizes gradually.

## 5. Discussion

Riquelme et al. (2014) proposed a discontinuity identification method, but the traces were not extracted on the same DSM. In order to make a comparison, we extracted the traces from the intersection lines between the fitting planes of discontinuities and the rock mass surfaces based on the discontinuity detection results (e.g., Otoo et al. (2011) and Gigli and Casagli (2011)). Traces obtained by the discontinuity intersection method are shown in Fig. 23. It can be seen that the traces in Fig. 23 contain more fragmented information compared with the traces in Fig. 11. The shortcomings of the discontinuity intersection method can be

summarized as follows: (1) traces cannot fully be detected because of the absence of points at the intersection of discontinuity planes and rock mass surfaces, (2) traces are broken into fragmented segments, and (3) redundant trace segments are generated by uneven discontinuity surfaces.

As noted by Umili et al. (2013), the validity of the automated discontinuity trace mapping method could significantly decrease due to the presence of artificial edges (e.g., induced by blasting in tunnel excavation) mixed with natural edges. In our work, the influence of artificial edges could be mitigated by adjusting the parameters in the trace detection algorithm. For example, if the trace segments that belong to one trace are interrupted by the stripping rocks due to blasting, we can increase $\theta_3$ and $d$ in the trace segment connection step to connect trace segments in similar directions. Similarly, we can increase $\theta_4$ in the redundant trace segment removal step to reduce blasting-induced small traces. As shown in Fig. 20, small trace segments are connected and discontinuity traces become more continuous.

## 6. Conclusions

This paper described a new method for automated discontinuity trace mapping from a digital surface model (DSM). The proposed method has three advantages: (1) trace feature points are detected using the Normal Tensor Voting Theory, which is robust to noisy point cloud data; (2) four post-processing steps (i.e., trace feature point grouping, trace segment growth, trace segment connection, and redundant trace segment removal) are proposed to overcome segmentation of extracted traces and to achieve more linear and continuous traces; and (3) the whole process could be streamlined without human intervention, except the triangular mesh element size should be tuned according to the mesh resolution.

A sensitivity analysis is performed to identify the optimal parameters in the proposed method. In our cases, the optimal triangular mesh element size is between 5 cm and 6 cm; the optimal angle threshold in the growing algorithm is between 70° and 90°; the optimal angle threshold in the connecting algorithm is between 50° and 70°; and the distance threshold should be at least 15 times that of the mean triangular mesh element size.

The case study presented in this paper shows that the proposed method provides fast and effective measurements of discontinuity geometric parameters. This method could be used as a supplement to traditional direct fracture mapping and scanline surveying.

## Acknowledgments

The authors gratefully acknowledge support from the National Natural Science Foundation of China (NSFC 41272289 and 41130751), the Science and Technology Plan Project of the Ministry of Transport of China (2013318J02120).

## References

Alexa, M., Behr, J., Cohen-Or, D., Fleishman, S., Levin, D., Silva, C.T., 2003. Computing and rendering point set surfaces. IEEE Trans. Vis. Comput. Graph. 9 (1), 3–15.
Barton, N., Lien, R., Lunde, J., 1974. Engineering classification of rock masses for the design of tunnel support. Rock Mech. 6 (4), 189–236.
Crosta, G., 1997. Evaluating rock mass geometry from photographic images. Rock Mech. Rock Eng. 30 (1), 35–58.
Dimitrov, D., 2009. Geometric Applications of Principal Component Analysis (Ph.D. dissertation). Freie Universität Berlin, Berlin, Germany, p. 99.
Ferrero, A.M., Forlani, G., Roncella, R., Voyat, H.I., 2009. Advanced geostructural survey methods applied to rock mass characterization. Rock Mech. Rock Eng. 42 (4), 631–665.
Franklin, J.A., Maerz, N.H., Bennett, C.P., 1988. Rock mass characterization using photoanalysis. Int. J. Min. Geol. Eng. 6 (2), 97–112.
Garcia, D., 2010. Robust smoothing of gridded data in one and higher dimensions with missing values. Comput. Stat. Data Anal. 54 (4), 1167–1178.
Garcia, D., 2011. A fast all-in-one method for automated post-processing of PIV data. Exp. Fluids 50 (5), 1247–1259.
Gigli, G., Casagli, N., 2011. Semi-automatic extraction of rock mass structural data from high resolution LIDAR point clouds. Int. J. Rock Mech. Min. Sci. 48 (2), 187–198.
Hadjigeorgiou, J., Lemy, F., Cote, P., Maldague, X., 2003. An evaluation of image analysis algorithms for constructing discontinuity trace maps. Rock Mech. Rock Eng. 36 (2), 163–179.
Haneberg, W.C., 2008. Using close range terrestrial digital photogrammetry for 3-D rock slope modeling and discontinuity mapping in the United States. Bull. Eng. Geol. Environ. 67 (4), 457–469.
Kim, H.S., Choi, H.K., Lee, K.H., 2009. Feature detection of triangular meshes based on tensor voting theory. Comput.-Aided Des. 41 (1), 47–58.
Kulatilake, P.H.S.W., Wu, T.H., 1984. Estimation of mean trace length of discontinuities. Rock. Mech. Rock. Eng. 17 (4), 215–232.
Lemy, F., Hadjigeorgiou, J., 2003. Discontinuity trace map construction using photographs of rock exposures. Int. J. Rock Mech. Min. Sci. 40 (6), 903–917.
Li, X., Zuo, Y., Zhuang, X., Zhu, H., 2014. Estimation of fracture trace length distributions using probability weighted moments and L-moments. Eng. Geol. 168, 69–85.
Mauldon, M., 1998. Estimating mean fracture trace length and density from observations in convex windows. Rock Mech. Rock Eng. 31 (4), 201–216.
Medioni, G., Lee, M.S., Tang, C.K., 2000. A Computational Framework for Segmentation and Grouping, 1st ed. Elsevier, Amsterdam, p. 257.
MVTec Software GmbH, 2012. Halcon Version 11 [HDevelop Reference Manual]. Retrieved from ⟨http://www.mvtec.com/halcon/⟩.
Otoo, J.N., Maerz, N.H., Duan, Y., Xiaoling, L., 2011. LiDAR and optical imaging for 3-D fracture orientations. In: Proceedings of the 2011 NSF Engineering Research and Innovation Conference, Atlanta, Georgia.
Page, D.L., Sun, Y., Koschan, A.F., Paik, J., Abidi, M.A., 2002. Normal vector voting: crease detection and curvature estimation on large, noisy meshes. Graph. Model. 64 (3), 199–229.
Reid, T.R., Harrison, J.P., 2000. A semi-automated methodology for discontinuity trace detection in digital images of rock mass exposures. Int. J. Rock Mech. Min. Sci. 37 (7), 1073–1089.
Person, K., 1901. On lines and planes of closest fit to system of points in space. Philos. Mag. 2, 559–572.
Riquelme, A.J., Abellán, A., Tomás, R., Jaboyedoff, M., 2014. A new approach for semi-automatic rock mass joints recognition from 3D point clouds. Comput. Geosci. 68, 38–52.
Roncella, R., Forlani, G., Remondino, F., 2005. Photogrammetry for geological applications: automatic retrieval of discontinuity orientation in rock slopes. In: Electronic Imaging 2005, International Society for Optics and Photonics, pp. 17–27.
Sun, Y., Page, D.L., Paik, J.K., Koschan, A., Abidi, M.A., 2002. Triangle mesh-based edge detection and its application to surface segmentation and adaptive surface smoothing. In: Proceedings of the International Conference on Image Processing, Vol. 3, pp. 825–828.
Slob, S., Hack, H.R.G.K., Feng, Q., Roshoff, K., Turner, A.K., 2007. Fracture mapping using 3D laser scanning techniques. In: Proceedings of the 11th Congress of the International Society for Rock Mechanics, Lisbon, Portugal, Vol. 1, pp. 299–302.
Slob, S., 2008. Automated Rock Mass Characterisation Using 3-D Terrestrial Laser Scanning (Ph.D. dissertation). Delft University of Technology, Delft, Netherlands, p. 101.
Sturzenegger, M., Stead, D., 2009. Quantifying discontinuity orientation and persistence on high mountain rock slopes and large landslides using terrestrial remote sensing techniques. Nat. Hazards Earth Syst. Sci. 9 (2), 267–287.
Potsch, M., Schubert, W., Gaich, A., 2005. Application of metric 3D images of rock faces for the determination of the response of rock slopes to excavation. In: ISRM International Symposium-EUROCK 2005, Brno, Czech. Rep.
Umili, G., Ferrero, A., Einstein, H.H., 2013. A new method for automatic discontinuity traces sampling on rock mass 3D model. Comput. Geosci. 51, 182–192.
Vöge, M., Lato, M.J., Diederichs, M.S., 2013. Automated rockmass discontinuity mapping from 3-dimensional surface data. Eng. Geol. 164, 155–162.
Wang, X.C., Cao, J.J., Liu, X.P., Li, B.J., Shi, X.Q., Sun, Y.Z., 2012. Feature detection of triangular meshes via neighbor supporting. J. Zhejiang Univ. Sci. C 13 (6), 440–451.
Zhu, H., Zuo, Y., Li, X., Deng, J., Zhuang, X., 2014. Estimation of the fracture diameter distributions using the maximum entropy principle. Int. J. Rock Mech. Min. Sci. 72, 127–137.
Zhang, L., Einstein, H.H., 1998. Estimating the mean trace length of rock discontinuities. Rock Mech. Rock Eng. 31 (4), 217–235.
Zhang, L., Einstein, H.H., 2000. Estimating the intensity of rock discontinuities. Int. J. Rock Mech. Min. Sci. 37 (5), 819–837.